Computer Aided Surgery 3:271–288 (1998)

Biomedical Paper

FRACAS: A System for Computer-Aided Image-Guided Long Bone Fracture Surgery

Leo Joskowicz, Ph.D., Charles Milgrom, M.D., Ariel Simkin, Ph.D., Lana Tockus, M.Sc., and Ziv Yaniv, M.Sc.

Institute of Computer Science, The Hebrew University of Jerusalem (L.J., L.T., Z.Y.), Departments of Orthopaedic Surgery (C.M.) and Experimental Surgery (A.S.), Hadassah University Hospital, and Biomedicom (L.T.), Jerusalem, Israel

ABSTRACT This article describes FRACAS, a computer-integrated orthopedic system for assisting surgeons in performing closed medullary nailing of long bone fractures. FRACAS's goal is to reduce the surgeon's cumulative exposure to radiation and surgical complications associated with alignment and positioning errors of bone fragments, nail insertion, and distal screw locking. It replaces uncorrelated, static fluoroscopic images with a virtual reality display of three-dimensional bone models created from preoperative computed tomography and tracked intraoperatively in real time. Fluoroscopic images are used to register the bone models to the intraoperative situation and to verify that the registration is maintained. This article describes the system concept, software prototypes of preoperative modules (modeling, nail selection, and visualization), intraoperative modules (fluoroscopic image processing and tracking), and preliminary *in vitro* experimental results to date. Our experiments suggest that the modeling, nail selection, and visualization modules yield adequate results and that fluoroscopic image processing with submillimetric accuracy is practically feasible on clinical images. Comp Aid Surg 3:271–288 (1998). ©1999 Wiley-Liss, Inc.

Key words: **computer-aided orthopedic surgery, trauma, long bone fracture reduction, fluoroscopic image processing**

INTRODUCTION

Background

Current orthopedic practice relies heavily on fluoroscopic images to perform a variety of surgeries such as fracture reduction, pedicle screw insertion, total hip replacement, and osteotomies, to name a few. Fluoroscopic images are used intraoperatively to determine the position of anatomy, surgical tools, and implants relative to one another; to monitor the advance of guide wires, drills, and reamers; and to make corrections as necessary. Figure 1 illustrates the use of fluoroscopy in closed medullary nailing for bone fracture reduction.

Although inexpensive and readily available, fluoroscopy has several important limitations. Fluoroscopic images are static, two-dimensional (2D), uncorrelated projections of moving spatial structures. Significant skills are required by the surgeon to mentally recreate the spatiotemporal intraoperative situation and maintain hand–eye coordination while performing surgical gestures. The surgeon's reduced capability leads to positioning errors and complications in a non-negligible number of cases.

Received July 12, 1998; accepted March 2, 1999.

Address correspondence/reprint requests to: Leo Joskowicz, Ph.D., Institute of Computer Science, The Hebrew University of Jerusalem, Givat Ram, Jerusalem 91904, Israel. E-mail: josko@cs.huji.ac.il

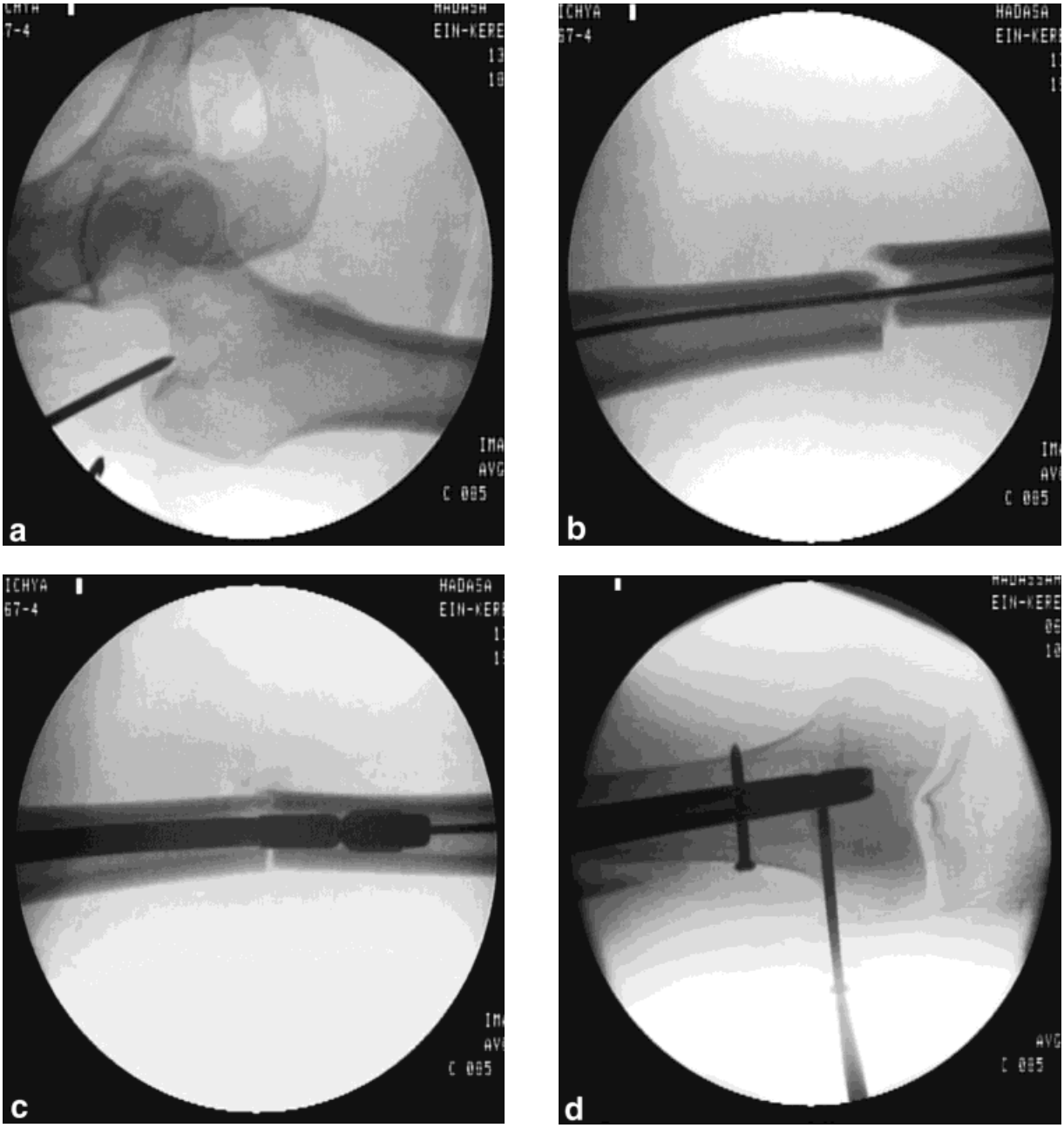

Fig. 1. Fluoroscopic images showing the steps of closed medullary nailing. **a:** opening of the medullary canal; **b:** alignment of the bone fragments; **c:** nail insertion; and **d:** distal locking.

Because the images are static and their field of view is narrow, frequent use of the fluoroscope is necessary, leading to significant cumulative radiation exposure to the surgeon. Each minute of exposure (about 60 shots) produces 4 rads of radiation, the equivalent of one computed tomography (CT) study[32]; many procedures require up to 30 min of exposure. Fluoroscopic images also show significant geometric distortion of up to several millimeters and varying exposure between shots, precluding their use for quantitative measurements and accurate navigation.

We are currently developing a computer-integrated orthopedic system, called FRACAS (Fracture Computer-Aided Surgery), for closed medullary nailing of long bone fractures. Closed reduction of fractures is the most common orthopedic trauma surgery, numbering over 400,000

cases/year in the United States alone. We chose closed medullary nailing as the focusing application for our research in developing computer-aided systems for fluoroscopy-based orthopedic procedures because it is the most common trauma procedure, it has great potential for reducing exposure and improving outcomes, and its accuracy requirements are possibly less stringent than those of other orthopedic procedures.

Closed medullary nailing is currently the routine procedure of choice for reducing long bone fractures.[3] It restores the integrity of the fractured bone by means of a nail inserted in the medullary canal. The concept behind closed fracture surgery is to perform internal fixation of the fracture without surgically opening the fracture site, thereby avoiding additional surgical trauma to the already traumatized area. In closed medullary nailing, the nail is placed without surgically exposing the fracture through an opening close to the piriformus fossa in the proximal femoral bone. The surgeon manually aligns the bone fragments by manipulating them through the leg, inserts a guide wire, reams the canal if necessary, and drives the nail in with a hammer. Lateral proximal and distal interlocking screws are inserted to prevent fragment rotation and bone shortening. Placing the distal screws is difficult because the nail deforms by up to several millimeters when inserted.[10] All these steps are performed under fluoroscopic guidance (Fig. 1).

The most common errors and complications in closed medullary fixation come from limited viewing capabilities. Because all alignment, reaming, and positioning must be done under fluoroscopy, the surgeon must mentally reconstruct the location of the parts in space and time, manipulate the tools and the bone fragments without direct visual feedback, and confirm the position with a new set of fluoroscopic images. This often imprecise, slow, and tedious procedure can cause improper positioning and alignment, inadequate fixation, malrotation, bone cracking, cortical wall penetration, and bone weakening with multiple or enlarged screw holes in the worst case. The surgeon's direct exposure to radiation in each procedure is between 3 and 30 min, with 31–51% spent on distal locking,[32] depending on the patient's anatomy and the surgeon's skill. When the bone fragments are difficult to align, the surgeon reverts to open techniques.

Femoral shaft fracture treatment is considered a surgical emergency, with fracture fixation recommended within 12 hours of the time of the fracture. Therefore, many of these surgeries are performed in the late evening and early morning hours, when the surgeon may be tired and his or her hand–eye coordination is suboptimal. The lack of registration between the surgeon's visual and mechanical sensory information causes a severe mental burden during the operation and contributes to a long learning curve in acquiring skills. The surgeon's cumulative radiation exposure, the reported number of complications, the proven record and high volume of closed femoral nailing, and the limitations of the current instrumentation motivated our search for improved computer-based solutions.

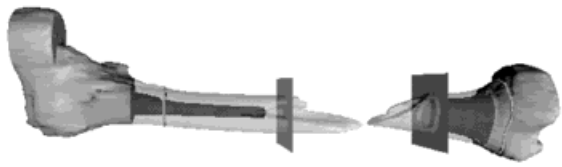

Fig. 2. Intraoperative 3D display of the distal and proximal bone fragments that replaces the fluoroscopic images. Their location is tracked and updated in real time during surgery.

The goals of FRACAS are to reduce the surgeon's cumulative exposure to radiation and improve the positioning and navigation accuracy by replacing uncorrelated static fluoroscopic images with a virtual reality display of 3D bone models created from preoperative CT and tracked intraoperatively in real time. Fluoroscopic images are used for registration—establishing a common reference frame—between the bone models and the intraoperative situation, and to verify that the registration is maintained. Figure 2 shows the virtual model of the bone fragments, which will replace the fluoroscopic images in Figure 1.

This article describes the system concept, software prototype, and preliminary experimental results to date. To motivate the specific goals and rationale of our approach, we begin by reviewing previous work on computer-based systems for fluoroscopic orthopedic procedures. We then describe FRACAS's hardware and software architecture and the protocol of the computer-aided surgery. The following section describes the main software modules: bone modeling and validation, visualization, preoperative planning, fluoroscopic image processing (dewarping, calibration, and contour extraction), tracking, and preliminary work on 2D/3D registration. We also describe an adjustable drill guide device for helping the surgeon in distal screw locking. We then describe preliminary experimen-

tal results for the different modules. We conclude with a discussion of current and future work on anatomy-based registration, tracking, and system integration.

Previous Work

Recent research shows that computer-aided systems can significantly improve the efficacy of fluoroscopy-based orthopedic procedures. The systems enhance, reduce, or altogether eliminate fluoroscopic images, replacing them with a virtual reality view in which the anatomy and instruments' positions are continuously updated as they move. Bone and instrument intraoperative positions are tracked in real time, usually with an optical tracking system, by attaching to them light-emitting diodes (LEDs). We distinguish among three classes of systems: (a) CT-based systems, which use a preoperative CT study to create a 3D anatomical model; (b) fluoroscopy-based systems, which use a few enhanced fluoroscopic images instead of hundreds; and (c) CT and fluoroscopy systems, which use both modalities.

Computed-tomography-based systems, which are the majority, replace fluoroscopic images with a virtual reality display of 3D bone and instrument models. The bone surface models are constructed for each patient from preoperative CT data. The instrument and implant geometric models are provided by their manufacturers. After elaborating a preoperative plan with these models, the bone and instrument preoperative and intraoperative positions are brought into alignment (registered), and their changing positions and orientations are followed in real time. The registration is performed with implanted fiducials or by intraoperatively acquiring points on the surface of the bone ("cloud-of-points" registration). Passive and semiactive mechanical supports for tool positioning and active cutting robots can be also integrated. Examples include total hip replacement systems for canal milling (ROBODOC[36]) and acetabular cup placement (HipNav[35]); systems for total knee arthroplasty[7] and total knee replacement[25]; and ACROBOT[5]; and systems for pedicle screw insertion,[22,27,28] iliosacral screw placement,[10] pelvic osteotomies,[21] and pelvic fracture reduction.[4] The strength of CT-based systems is that they produce the most accurate 3D geometric models.

In fluoroscopy-based systems,[2,16,30] a few enhanced fluoroscopic images at carefully chosen viewpoints and moments are acquired, corrected for geometric distortion, calibrated, and correlated. The images are used to determine the initial relative spatial position of instruments and bones, and to approximate continuous fluoroscopy by repositioning in real-time 2D contour models of instruments based on the tracking data. The advantage of this virtual fluoroscopy technique is that it is closest to the current clinical procedure: It is simple to use, has moderate equipment requirements, works directly on intraoperative data, and does not require a preoperative CT study. The models, however, are not always complete and are possibly less accurate than those derived from CT data. Procedures under study include intramedullary nailing, distal locking, percutaneous discectomy, transpedicular and dynamic hip screw placements,[30] removal of osteonecrotic lesions, canal drilling for graft positioning, pelvis tumor biopsies, and osteotomies.[2]

Computed-tomography- and fluoroscopy-based systems are like CT-based systems except that fluoroscopic images are used to register the preoperative CT model to the intraoperative situation based on the bone surface model and its projection in the fluoroscopic images. This type of anatomy-based registration is essential when other methods, such as attaching external fixators, implanting fiducials, or obtaining data points by direct contact on the surface of the bone, are impractical or impossible. Examples include systems for revision total hip replacement[18,37] and for closed medullary nailing.[19] These types of systems aim to combine the advantages of CT-based systems with anatomy-based registration at the expense of additional CT or fluoroscopy. Image-based registration is highly desirable since it does not require implanted fiducials or direct contact with the anatomy, which is not possible in a variety of closed and percutaneous procedures. Performing automatic, accurate 2D/3D anatomical registration is a challenging task which has yet to find a satisfactory solution.[13–15,23,24]

Two computer-based systems specifically designed for long bone fracture reduction[30,41,16] are fluoroscopy-based systems which focus exclusively on assisting the surgeon in distal screw locking. Phillips et al.[30] and Viant et al.[41] incorporated a passive mechanical arm with optical encoders to guide the surgeon to the right drilling position. The system automatically identifies the distal holes in the fluoroscopic images, plans the drilling trajectory, and constrains the passive arm motions. The advantage of this system is that it eliminates trial-and-error drill positioning, although it requires additional mechanical hardware. The system of Hofstetter et al.[16] continuously displays the projection of the surgical tools as they move on preselected

fluoroscopic images. Since the images are correlated, the surgeon can simultaneously view the tool progression from several viewpoints. None of these systems provides preoperative planning support, or 3D views of the bone fragments and tools updated in real time.

Accuracy and clinical outcome assessment are of great importance for evaluating computer-aided orthopedic surgery systems. *In vitro* and *in vivo* clinical accuracy evaluations have recently been performed for CT-based systems.[11,12,17] Simon[34] and Ellis et al.[6] proposed mathematical models and algorithms for accuracy evaluation of CT-based registration using fiducials and surface models. These results indicated that worst-case clinical submillimetric accuracy is attainable. Much experimentation and research is still necessary for fluoroscopy-based systems.

Goals, Rationale, and Novelty

Our goal in developing FRACAS is to assist the surgeon in all the steps of fracture reduction, not just in distal locking. The system provides 3D bone modeling, preoperative planning, fluoroscopic image processing, and anatomy-based 2D/3D registration of the bone fragment models using fluoroscopic images. The expected benefits of the system are:

1. Substantial reduction of the surgeon's cumulative exposure to radiation
2. Reduction of surgical complications associated with alignment and positioning errors of bone fragments, nail insertion, and distal screw locking
3. Improvement of the chances of completing the surgery closed
4. Improvement of the surgeon's hand–eye coordination and reduction of the surgeon's mental burden in registering his or her visual and mechanical reference frame
5. Reduction of overall intraoperative time, especially for distal locking, and reduction of surgeon fatigue
6. Improvement of preoperative planning, i.e., fracture assessment and nail selection
7. Reduction of the skill acquisition learning curve.

To achieve these goals, we chose to develop an integrated CT and fluoroscopy–based system to assist the surgeon in all the steps of intramedullary nailing: preoperative nail selection, bone fragment alignment, and distal locking. While nail size selection and distal locking can be done with 2D X-ray images, distal and proximal bone fragment canal alignment most likely cannot, since it involves relatively large, loosely coupled spatial motions that are hard to visualize with 2D projections. Also, our experiments show that extracting the canal contour from fluoroscopic images is more difficult and less reliable than extracting it from CT data. Preoperative nail selection and distal locking can only benefit from the higher quality of the models derived from CT. Distal locking might be feasible with intraoperative fluoroscopic images alone, as proposed by others,[16,29,30,41] since spatial motions are relatively small. However, if the CT is already available, it is well worth using it since it provides a 3D virtual reality view which eases the drill positioning.

We believe that the additional cost and time of the preoperative CT study are outweighed by the potential reduction in more expensive intraoperative time, in minimizing mistakes and repetitive attempts at fracture reduction, and in reducing the surgeon's exposure to radiation. In many centers, including ours, CT is readily available for trauma patients, adding little preoperative time, risk, and morbidity. Cases of fractured femur may be divided into those in which the sole injury is the fractured femur and those in which there is multiple trauma. Multiple trauma patients are likely to have other CT studies done anyway (e.g., of the abdomen and pelvis). In both cases, the patient's leg is immobilized on a Thomas splint, which makes transport on the emergency-room stretcher and transfer to the CT table easy and relatively pain free, with minimal fracture movement. Any fracture movement that does occur would not be associated with an increased risk for pulmonary embolism.

MATERIALS AND METHODS

FRACAS: System Description and Protocol

The FRACAS system[19] is composed of four units: (a) a standard fluoroscopic C-arm, (b) a real-time optical position tracking system, (c) a computer workstation with data-processing and visualization software, and (d) an adjustable drill guide device for assisting the surgeon in distal locking. The fluoroscopic unit captures the images that are used to establish a common reference frame (registration) between the intraoperative bone position and preoperative bone fragment models. The tracking unit provides accurate, real-time spatial object positions with optical cameras following infrared LEDs rigidly mounted on the surgical instruments

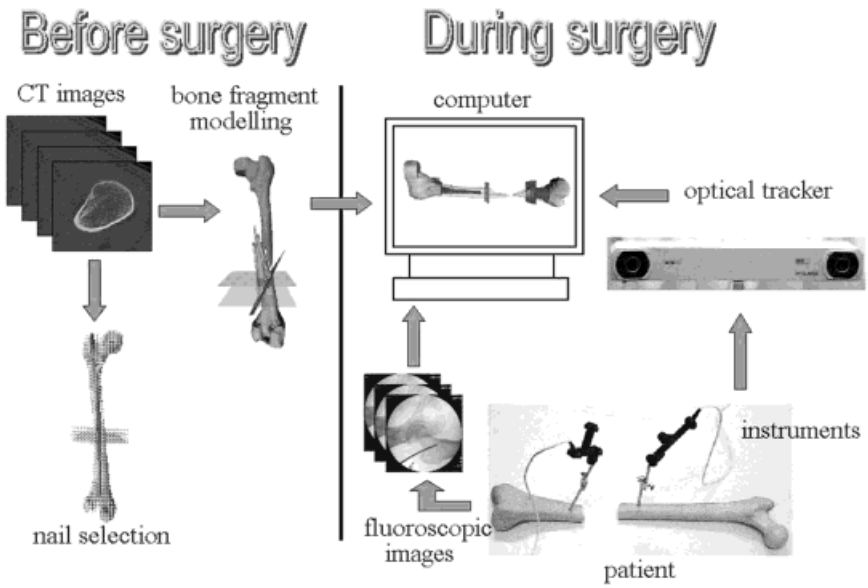

Fig. 3. FRACAS system concept: Preoperatively, a CT scan is acquired and 3D proximal and distal bone models are constructed. During surgery, the proximal and distal bone models are shown on the computer screen. The position of the 3D models is tracked in real time with an optical tracking system. Fluoroscopic images are used to register the preoperative and intraoperative situation.

and attached to the bones via bone screws.[22,28] The computer workstation is used preoperatively for modeling and planning, and intraoperatively for data fusion and display. The adjustable drill guide device is a passive positioning device that attaches to the nail head to assist the surgeon in distal hole drilling. Figure 3 illustrates the system concept.

The envisaged sequence of the procedure is as follows. Preoperatively, a CT of the healthy and fractured bones is acquired. The preoperative CT data sets can have different slice spacing in different areas to achieve the best compromise between the number of slices and the required accuracy. Surface and canal bone models of the distal and proximal bone fragments to be joined are then constructed by the modeling module. Using the planning modules, the surgeon interactively selects the distal and proximal bone fragments and nail type, length, and diameter. Shortly before the surgery, the fluoroscopic unit is calibrated at predefined orientations by a technician. The patient is then brought into the operating room and the surgeon prepares and exposes the femoral canal following the usual procedure.

To track the position of the distal and proximal bone fragments, the surgeon rigidly implants two custom bone screws with LEDs attached to them (Fig. 4). The bone screws are placed in each of the two bone fragments near the fracture site so as not to obstruct the insertion of the nail. With the LEDs in place, the technician activates the optical tracking system to capture the location of the bone fragments and surgical instruments at the predetermined C-arm orientations. Fluoroscopic images are then captured by a technician (without the nearby presence of the surgeon) to perform two anatomy-based registrations with each of the preoperative proximal and distal bone fragment models. The images are imported into the workstation via a video frame grabber, and the tracking data via a serial port. The visualization module constructs the virtual reality image showing the bone fragments and surgical instrument models and presents it to the surgeon on a high-definition monitor.

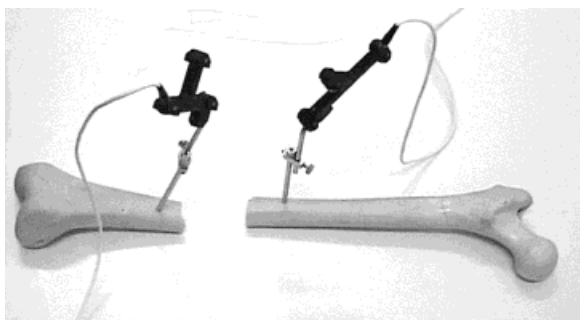

Fig. 4. Proximal and distal bone fragments with bone screws and active tracking device attached to them.

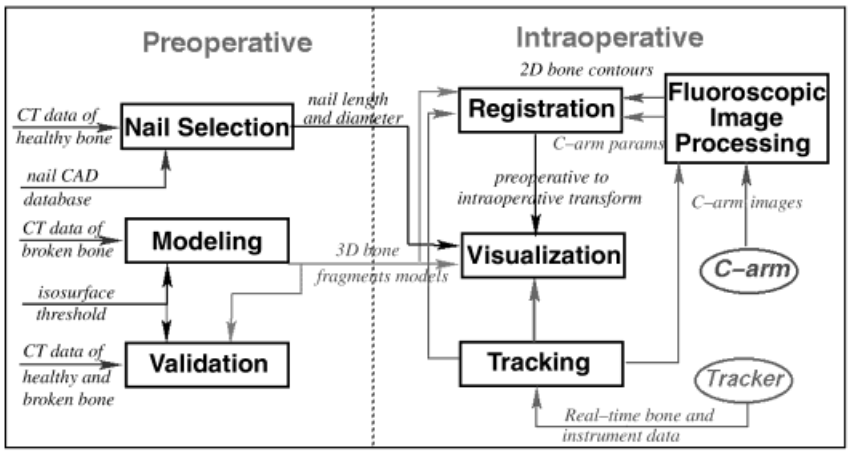

Fig. 5. Flow diagram of FRACAS's main software modules.

During surgery, the surgeon manipulates the bone fragments and surgical tools, following their relative positions and orientations on the monitor. Once the desired positioning is achieved, a new set of fluoroscopic images is captured and registered to confirm the intraoperative situation with the displayed model. This process is repeated for the different steps of the procedure. For distal interlocking of the intramedullary nail, the surgeon attaches the drill guide to the nail head, adjusts its length and entry angle based on new fluoroscopic images, and locks it in place to allow accurate drilling of the distal holes for the interlocking screws, with no further radiation exposure to the surgeon's hands.

Figure 5 shows the main FRACAS software modules and the data flow between them. The modeling module constructs 3D surface models of selected proximal and distal bone fragments from CT data of the broken bone. These models will be shown intraoperatively to the surgeon. The nail selection module assists the surgeon in determining the optimal nail type, size, and length when a CT of the healthy bone is available. The validation module helps the surgeon to verify visually that the computed surface model closely matches the CT data. The visualization module provides the surgeon with a virtual reality view of the intraoperative position and orientation of the proximal and distal fragments. The fluoroscopic image processing module calibrates the C-arm, corrects the fluoroscopic images for distortions, and extracts the bone contours so they can be matched to the 3D bone fragment models by the registration module. The registration module finds the intraoperative locations of the proximal and distal bone fragments with respect to the preoperative 3D model by minimizing for each the distance discrepancy between the 2D and 3D contours. The tracking module processes the location data provided by the tracking unit and passes it on to the visualization module to update in real time the intraoperative view. In the following, we describe all the modules in detail. A first working prototype of all the modules has been implemented, with the exception of the registration module, which is currently under development. See Tockus[38] and Yaniv[44] for detailed descriptions of the modules.

Modeling, Visualization, and Preoperative Planning

The preoperative modules have been designed so that the surgeon can use them after minimal training without the help of a technician.

Modeling and Validation

The modeling module inputs the CT data and a user-defined bone density threshold value, and outputs inner and outer surface models of selected proximal and distal bone fragments. The models are produced by first creating polygonal surface models of the bone external and internal fragment surfaces. This process usually lumps together bone fragments that are in contact owing to the action of the muscles, producing a single connected piece for linear fractures, or several pieces for segmental and comminuted fractures. Since threshold information by itself is not sufficient to determine when a new fragment begins or ends, the surgeon interactively defines the extent of the fragments of interest with

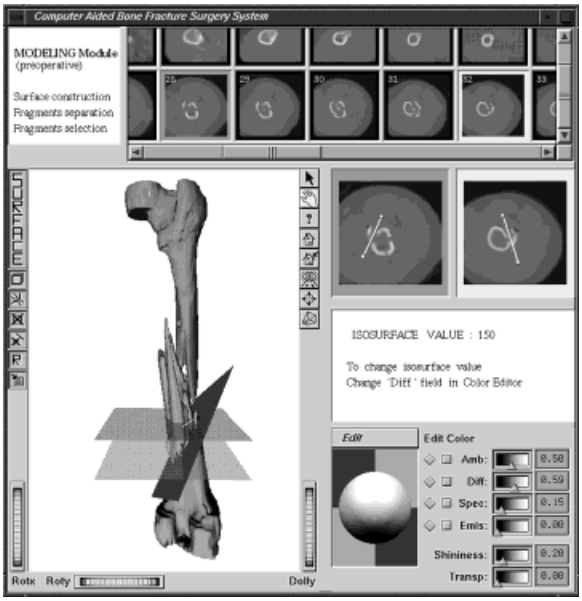

Fig. 6. The Modeling module display. The top window shows the original CT slices. The left bottom window shows the surface model of the fractured bone (the canal surface is hidden). The horizontal planes indicate the position of the selected CT slices shown in detail on the two windows on the right. The slanted plane is the user-defined cutting plane that separates the bone fragments. The bottom right window shows the bone density threshold and the material and viewing parameters.

successive cutting rectangles whose intersection defines regions of interest. Figure 6 shows the modeling module window with a segmental comminuted fracture.

The bone fragment surface models are connected meshes of triangles and are extracted from the CT data using an extended marching cubes algorithm.[26] The slice spacing in the CT data set need not be uniform. Our algorithm automatically classifies surface triangles as belonging to the bone outer surface or the canal according to threshold values. The size of the resulting meshes depends on the resolution of the CT data. For example, the CT set in Figure 6 consists of 44 slices at 10-mm intervals, image size 160 $\times$ 160, pixel size 1 mm^2; it yields a model of about 75,000 triangles. Models with up to 200,000 triangles are obtained by using slices at 4-mm intervals.

The fragment models are separated into different pieces by means of user-defined cutting planes whose intersection defines regions of interest. A cutting rectangle is created in one of two ways. One is by defining it in a default configuration and bringing it to the desired location using manipulation dials. A better way is to interpolate it from two line segments defined in two CT slices close to the area of the desired separation (the white line segments in the two detailed CT windows on the right in Fig. 6). To avoid separating model parts that are far from the cutting area, the plane is automatically clipped to a rectangle. Its position can then be interactively fine-tuned by changing the position of the segment end points or by using the manipulation dials. Either way, the bone fragments are then separated according to their point membership classification relative to each plane. By repeatedly positioning and sizing the clipping rectangle, the extent of the distal and proximal bone can be easily determined by the surgeon. Undesired bone fragments and bone particles are eliminated by clicking on them with the mouse. To verify that the computed surface model closely matches the CT data, we developed a visual validation module. For each CT slice, the module computes the cross section of the geometric model at the CT slice location and shows it superimposed with the original CT data. To improve the fit, the bone density threshold value can be adjusted.

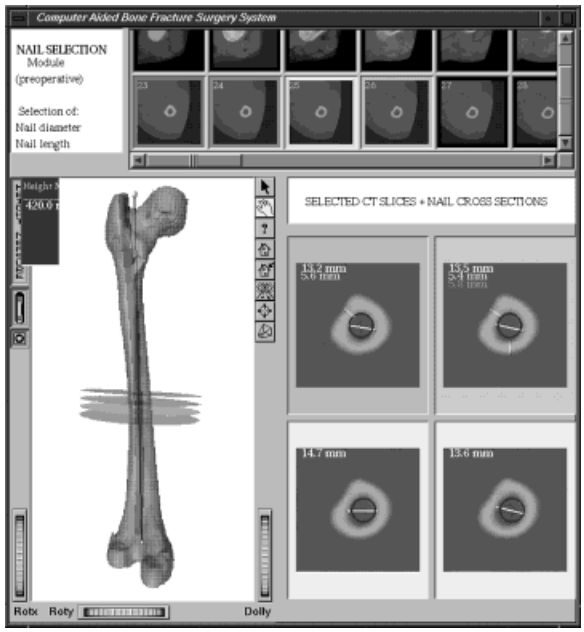

Fig. 7. The Nail Selection module display. The top window shows the original CT slices. The left bottom window shows the healthy bone surface model, the selected nail model, and the planes of the four selected CT slices shown in detail on the four windows to the right of it. The detailed CT slices windows on the right show the nail cross section (dark circle) superimposed on the original CT image.

Nail Selection

The nail selection module assists the surgeon in determining the optimal nail type, size, and length when a CT of the healthy bone is available (Fig. 7). To choose a nail, the surgeon interactively performs diameter and height measurements on the CT slices and on the reconstructed 3D bone model. Canal diameter measurements are performed on the CT slices (four right windows in Fig. 7) by moving the end points of a measuring segment (shown in white). Its length is interactively updated and appears in the top left corner of the window. Height measurements are performed on the 3D window (left window) by moving the end points of the measuring segment (black segment). Its length is interactively updated and appears in the top left corner of the window. Having determined the closest standard diameter and nail length, the system retrieves and displays the corresponding nail from a predefined CAD library of nail models available at the site. The surgeon can then interactively position the nail in its inserted position and verify that it fits in the canal and that there is no impingement on the knee or hip joints. Although the actual nail deforms by several millimeters when it is inserted into the canal,[10] the displayed nail position is close enough for preoperative evaluation and selection.

Visualization

The visualization module provides the surgeon with a virtual reality view of the intraoperative position and orientation of the proximal and distal fragments, the nail, and the surgical instruments. The positions are updated with real-time data from the tracking unit, after the preoperative model and the intraoperative situation have been registered (Fig. 2). When aligning the proximal and distal canal, FRACAS displays the central part of the exterior bone fragments translucid and highlights the canal surface inside. The femoral head and the condyles are displayed as opaque to provide a reference frame for the joint and bone axes. When doing the distal nailing, the drill tip and position of the distal holes, obtained from fluoroscopic images, also appear in the image. The virtual reality window provides standard viewing capabilities such as zooming, viewpoint, and perspective modification. Cross sections of the bone can be visualized by placing cutting planes which can be interactively moved up and down the bone as desired.

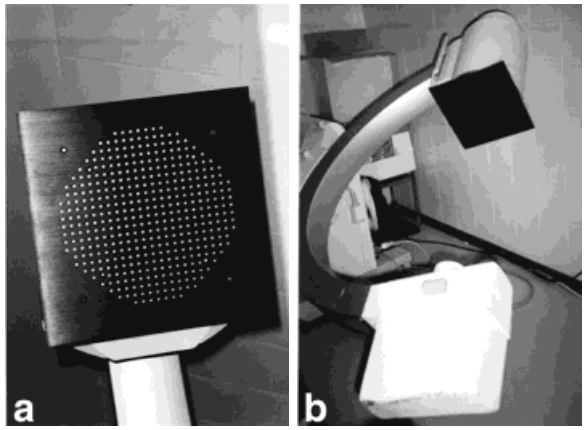

Fig. 8. Dewarping grid mounted on the C-arm image intensifier. **a:** grid; **b:** mounting on C arm.

Fluoroscopic Image Acquisition and Processing

To use fluoroscopic images for accurate anatomy-based registration, it is necessary to correct them for distortion, obtain the camera parameters, and extract the bone contours to be matched with projections of the 3D bone fragment models. The main difficulties are that the images have limited resolution, exhibit nonuniform exposure variation across the field of view, and have varying contrast and exposure from shot to shot. In addition, the distortion pattern and camera parameters are orientation dependent and vary from unit to unit and session to session, so they must be obtained at a set of predefined orientations by imaging custom-built distortion and calibration phantoms shortly before the surgery begins. While many methods for distortion correction, camera calibration, and contour extraction are described in the literature, our method emphasizes integration, full automation, simplicity, robustness, and practicality. It focuses on fluoroscopic bone images and their use in 2D/3D anatomy-based registration. While the dewarping and camera calibration parameters can be obtained simultaneously, we chose, as have many others, to decouple them and thus obtain simpler methods that yield more accurate and robust results.

FRACAS fluoroscopic image acquisition protocol proceeds as follows. Shortly before the surgery, the X-ray technician attaches a custom-built dewarping grid and calibration object to the image intensifier plate via existing screw holes (Fig. 8). One pair of images of the phantom objects is acquired at predefined C-arm orientations, and its corresponding dewarp maps and calibration param-

eters are computed and stored for use during surgery. We capture between six and 10 pairs of images at evenly spaced orientations for registration and lateral and anterior–posterior pairs for position validation during surgery. The pitch and yaw orientations of the C arm are read off the C-arm scale attached to the frame, which is accurate to within a few degrees. Preliminary results indicate that the imaging errors incurred by the inaccuracy of manually returning the C-arm to a predefined position to within a few degrees are below 0.5 mm. However, if further testing indicates that the error is too large, we will attach LEDs to the C-arm, as in Brack et al.[2] and Hofstetter et al.,[16] and use the tracker's reading to return to the predefined orientations more accurately. This procedure, which should last about 15–20 min, will be carried out by the X-ray technician and does not add time to the surgical procedure.

After the patient is brought into the operating room and the LEDs for optical tracking are in place, new fluoroscopic images are acquired at the predefined C-arm orientations. The C-arm's image intensifier is also equipped with LEDs to obtain the C-arm's position and orientation relative to the proximal and distal bone fragments and the surgeon's drill. After correction, camera calibration, and bone contour extraction, the registration module establishes a common reference frame for each of the proximal and distal bone fragments. The surgery then proceeds under FRACAS's virtual reality guidance. Before the critical steps of the reduction are performed (e.g., fragment alignment, nail passage from the proximal to the distal fragment, hole drilling for distal screw locking), additional fluoroscopic images are acquired, displayed, and used to correct the registration.

Image Dewarping

Fluoroscopic images present substantial distortion[2,8,16,33] owing to three factors: (a) The image intensifier receptor screen is slightly curved; (b) the surrounding magnetic fields of the earth and nearby instruments deflect the X-ray beam electrons; and (c) the C-arm armature deflects under the weight of the image intensifier, changing the focal length of the camera. The first effect can be modeled as radial pin-cushion distortion and is independent of the C-arm location. The second effect yields image translation and spatially variant rotation, and is C-arm orientation dependent. The third effect requires knowing the magnitude of the deflection. The distortion pattern resulting from all the three factors is present in all units, including modern ones, and varies from unit to unit and session to session, with up to 10 mm shift on the image edges.[33]

Fluoroscopic image dewarping has received considerable attention (see Fahrig et al.[8] for a review of the literature). It consists of computing a dewarp map from a reference image of a uniform grid of fiducials (e.g., steel balls or holes) attached to the image intensifier plate and from the known fiducial centers' geometric coordinates. The shift of each pixel in the image from its real projected location determines the amount of distortion. While the dewarping and camera calibration parameters can be obtained simultaneously, we chose, as have many others, to decouple them and thus obtain simpler methods that yield more accurate and robust results.

Global methods[8,20] model the distortion across the entire image as a single function (e.g., a bivariate polynomial) whose coefficients are determined by least-squares fitting of the image and geometric center coordinates. Local methods[16,33] model the distortion by tessellating the image field of view into triangles or quadrilaterals for which individual distortion functions are computed. The functions are determined by the distances between the image and the geometric ball center coordinates, usually by bilinear interpolation. The global method produces compact maps, but assumes that the distortion in the image is smooth and continuous. Local methods make no assumptions on the nature of the distortion and model it more accurately when it varies considerably across the field of view. Recently, Fahrig et al.[8] reported comparable results when using local bilinear interpolation and global fourth-order polynomials.

We chose local bilinear interpolation because of its simplicity, computational efficiency, and generality in modeling unknown distortions. The procedure is simple to use and, unlike some others, does not require user input for hole segmentation and center identification. The map is computed in four steps:

1. Fiducial identification. The program identifies the plate holes in the image from the background by automatically finding the gray-scale pixel value for hole segmentation from the image histogram. The gray-level histogram is relatively stable and varies little with different levels of image exposure. The program looks for two peaks, one in the histogram's low gray-level area, corresponding to the aluminum plate, and one in

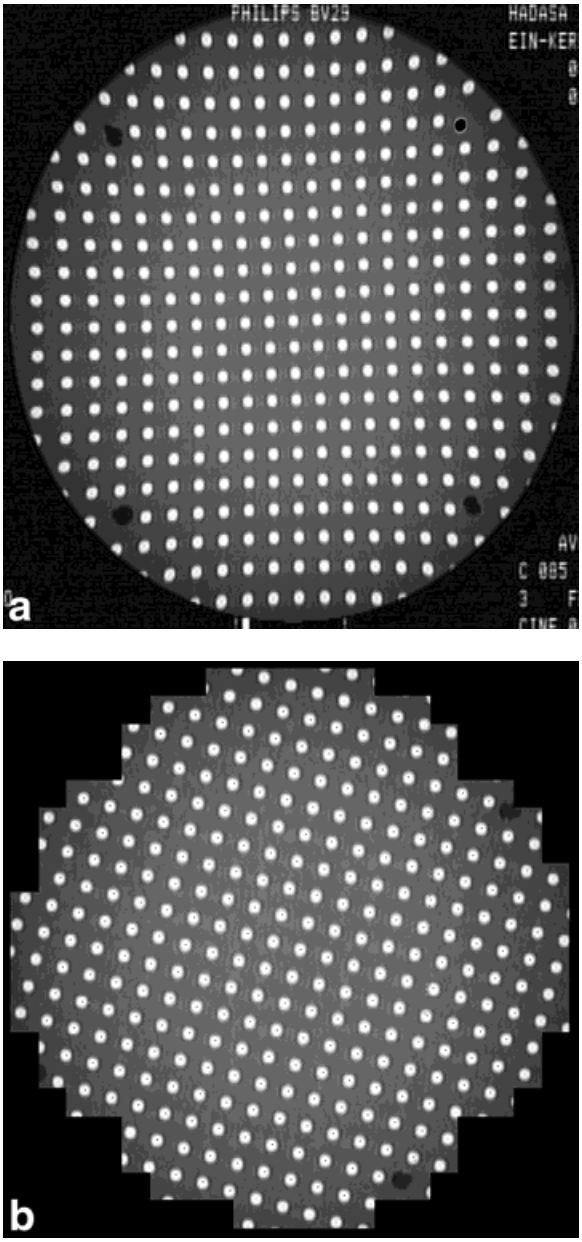

Fig. 9. Fluoroscopic images of the dewarping grid **a:** in its original position and **b:** in its new position after dewarping. Black dots mark detected hole center points.

the high gray-level area, corresponding to the holes.

2. Fiducial center computation. The coordinates of each fiducial center are computed to subpixel accuracy by weighted pixel gray-scale average.
3. Pairing of the image and geometric fiducial centers. The hole center of each image fiducial center is paired with the closest geometric fiducial center.
4. Correction computation. For each pairing, the correction from the distances between the image and geometric fiducial center coordinates is computed.

The program tessellates the field of view into quadrilaterals whose end points are the hole center points. It uses the bilinear radial function to compute the undistorted coordinates of each image pixel. The coefficients for each region are obtained by solving a set of eight linear equations expressing the distances from the quadrilateral end points.

New undistorted images are produced by computing for each pixel in the distorted image its new location and gray-scale value in the undistorted image according to the dewarp map. The gray-scale value of each new undistorted pixel is also obtained by pixel gray-scale value bilinear interpolation. Figure 9 shows an image of the dewarp plate before and after dewarping.

Camera Calibration

We use Tsai's 11-parameter pinhole camera model[40] and solution method to model the fluoroscopic camera. Since the parameters are pose dependent, we compute them for the same C-arm orientations as for dewarping. The parameters are the three relative positions, $T = T_x, T_y, T_z$, and orientations, $R = R_x, R_y, R_z$, of the pinhole with respect to the imaging plane; the focal length, f; the image center location, C_x, C_y; and the image scaling and radial distortion coefficients, s and κ. Because the images have been previously corrected, the radial image distortion assumption holds. We could set the image scaling and radial distortion parameters $s = 1$ and $\kappa = 0$, but we compute them anyway to further verify the dewarping procedure.

The set of equations relating the parameters is obtained by formulating the transformations from the world coordinate to the camera coordinate frames, transforming the 3D camera coordinates into 2D coordinates in an ideal undistorted image, and adding radial distortion, shifting, and scale. The equations can be solved in two steps, based on the radial alignment constraint. Following the camera calibration procedure for single-view noncoplanar points, the extrinsic parameters R and T, with the exception of T_z, are found by solving a set of linear equations. Based on these values, the remaining parameters are derived. While this method requires at least seven points, we use the least-squares method to incorporate more points. Figure 10 shows a photograph of the calibration object and its fluoroscopic image.

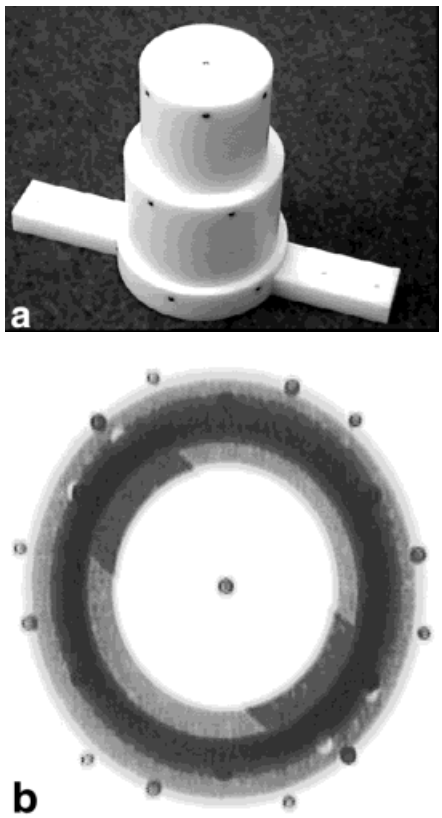

Fig. 10. **a:** Calibration object and **b:** its fluoroscopic image.

Contour Extraction

To extract bone contours reliably from fluoroscopic images, we developed a new bone contour segmentation algorithm based on robust image region statistics computation.[9] While many algorithms are available for contour extraction,[42] our experiments on clinical images showed that none of them produced satisfactory results. Edge detection techniques such as the Marr–Hilderth edge operator were overly sensitive to noise and nonuniform image exposure, producing too many false contours. The Canny edge detector yielded better results but required extensive threshold adjustments for every image, with frequent over- and undersegmentation. We ruled out the active contours techniques because they cannot detect overlapping contours, require an initial guess near the target, and are computationally expensive.[2] The region growing methods yielded better results but created many spurious boundaries because of the nonuniform exposure across the field of view.

Our new bone contour segmentation algorithm is based on robust image region statistics computation. Its main advantage over other methods is that it adaptively sets local segmentation thresholds from a robust statistical analysis of image content. Working on the gradient image, the algorithm starts from global threshold setting and performs region growing based on adaptive local thresholds and zero-crossings filtering. Because the algorithm uses both global and local thresholds, it is less sensitive to the exposure variations across the field of view. Pixels are classified into one of three categories—bone, candidate, or background—according to the number of pixels above a predefined percentile, and not according to a prespecified absolute value. The percentile indicates the number of pixels in the gradient image histogram with gray values below (background) or above (bone), with candidate pixels in between. Initial region classification is obtained with global percentile thresholds. To overcome the nonuniform exposure, the classification is adaptively updated with local percentile thresholds over a fixed-size window. Filtering the result with the original image zero crossings localizes the contour inside the region.

The contour segmentation algorithm inputs global and local, upper and lower percentile thresholds, and a window size. It finds edge pixels in four steps:

1. Initial global classification. Compute the gradient image and its histogram. Set the global threshold values according to the given global image percentiles. The gradient image pixels are classified according to the global thresholds as background (below the lower threshold), bone (above the upper threshold), or candidate (between the lower and upper thresholds).
2. Revised local classification. For each candidate pixel in the gradient image, place a local window of prespecified size centered at the pixel and compute the local thresholds from its histogram. The pixel label is modified according to the local threshold values.
3. Region growing and small components elimination. Recursively relabel as bone all pixels labeled candidate with one or more neighboring bone pixels (either the four- or eight-neighboring scheme can be used). Next, remove all connected bone pixel components with too few pixels (e.g., <50) by relabeling them as background; they are most likely noise.
4. Filtering with zero-crossings image. Compute the binary zero-crossings image of the

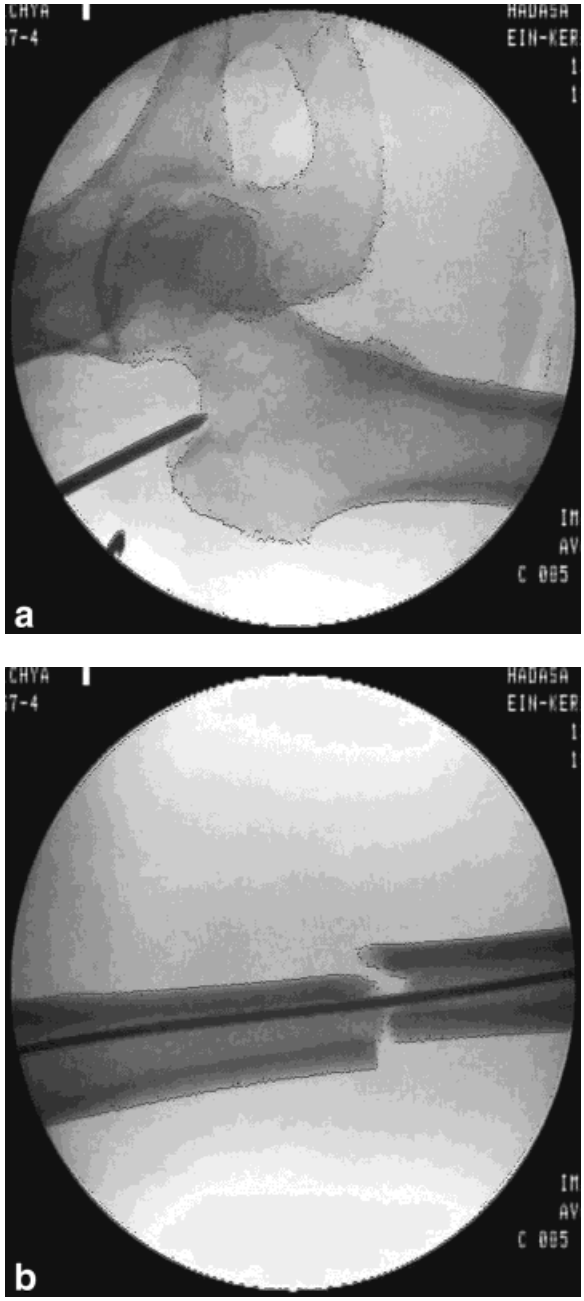

Fig. 11. **a,b:** Extracted pixel contours (black dots) of the first two fluoroscopic images in Figure 1. The contours of the metal tools were also segmented because metal density is higher than bone density.

original image and perform a binary AND operation with the labeled gradient image. The labeled gradient image is converted to a binary image by setting bone pixels to 1 and background pixels to 0. The results are the pixels on the bone contours. Figure 11 shows the contours extracted from two fluoroscopic images.

Tracking

For tracking the proximal and distal bone fragment models, the instrument position, and the C-arm orientation, we use the Hybrid Polaris system (Northern Digital, Canada) and active instruments and bone screws by Traxtal (TS032 locking screws, TT001-HRL active trackers) (Fig. 4). The tracking module is a simple interface between the tracker unit and the registration, visualization, and fluoroscopic image-processing modules. It includes functions to initialize the tracker, establish a connection, and transmit the instrument data.

Distal Locking

Once the nail has been inserted and the proximal screw has been locked into place, one or two screws are usually inserted in the distal part of the nail. The screws prevent shortening and rotation of the bone. Distal locking is challenging because, unlike the proximal lateral holes, the exact location of the distal holes is unknown. The nail bends to follow the canal shape by up to several millimeters, and its depth depends on how the surgeon inserted the nail.[10] Since it is not possible to determine preoperatively the exact locations of the distal holes, fluoroscopic images of the distal part of the nail showing the holes must be acquired and registered to the bone model.

We have designed and manufactured at the Precision Mechanics Laboratory, the Hebrew University of Jerusalem, a custom adjustable drill guide device to assist surgeons in distal locking (Fig. 12). The drill guide attaches to the nail's head like the proximal targeting device. It has four adjustable degrees of freedom which can be locked once the desired position and orientation have been found: length and orientation around the bone axis, and distance and orientation of the drill guide perpendicular to it. The tip has LEDs attached to it, so its position and orientation relative to the distal bone fragment can also determined in real time. To determine the relative position of the distal nail holes with respect to the 3D distal bone fragment contour, we plan to acquire AP and lateral distal images of the bone and nail, extract the hole axes and 2D bone contours, and match them with the registered 3D distal bone fragment model. By registering the tip of the positioning device with the bone contour, we establish a common reference frame between the target holes and the drill guides. The goal of the surgeon is then to align the nail holes and the drill guide hole axes following their spatial view on the computer screen.

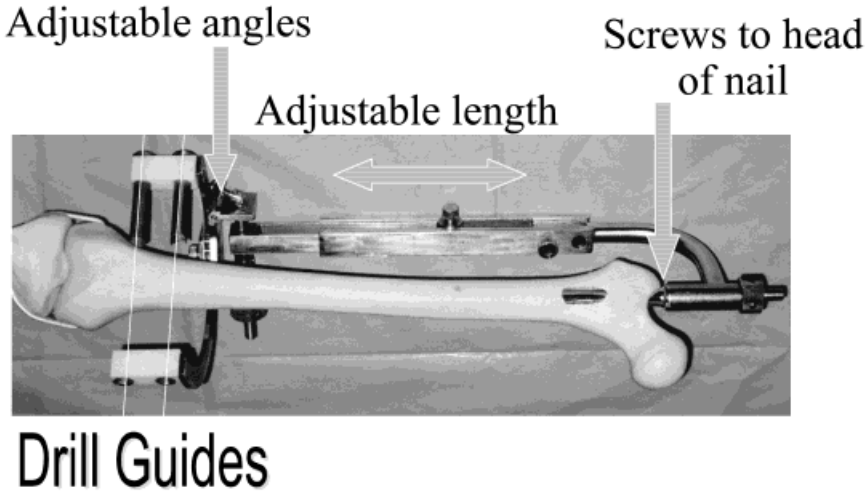

Fig. 12. Prototype of adjustable drill guide device for assisting surgeons in distal locking. The device is shown mounted on a dry bone.

Anatomy-Based 2D/3D Registration

Registration is a key step to establishing a common reference frame between the intraoperative proximal and distal bone models and the intraoperative situation. Existing systems rely on implanted fiducials[26] or direct contact with the bone surface ("cloud-of-points" method)[21,27,28,35] to establish a rigid registration between the preoperative models and the intraoperative anatomy. These techniques are impractical for closed medullary nailing: Implanting six fiducials in trauma patients (three for the proximal and three for the distal bone fragments) is clearly undesirable. Direct contact with the bone surface is not feasible for the distal bone fragment unless an additional opening in the skin is made. Thus, the only viable alternative is to use fluoroscopic images of the bone fragments to determine their actual position and orientation.

Anatomy-based registration of 2D X-ray images to 3D models[13–15,22] consists of matching a set of rays emanating from the camera focal point and going through the image contour points. When registered, the rays graze the surface of the 3D model, so the goal is to find a transformation that brings the 3D model surface as close to the rays as possible.

We plan to use the contours of the femoral head and condyles for registration because the anatomical structures are more complex in these areas and thus less ambiguous when viewed at different angles. Also, our preliminary results on X-ray image segmentation show that it is very difficult to extract contour information from the canal or near the fractured area. In the CT study, we plan to acquire more slices in those areas (4–6-mm spacing) and less in the fracture area (8–10-mm slices).

We are currently exploring an extension of the iterative closest point method[1] using restricted octrees for fast distance computation,[23] and nonnegative least squares for approximate distance minimization.

RESULTS

Preliminary Experiments

To validate the modeling, visualization, and nail selection modules, we acquired and processed six sets of CT data of trauma patients under clinical conditions. The fractures varied from simple transverse fractures (Fig. 1) to segmental comminuted fractures (Fig. 6). Between 75 and 150 slices of both legs were acquired for each at different intervals (2, 4, and 8 mm) in different zones, as explained earlier. For each, FRACAS constructed models for the healthy and bone fragment models and the surgeon selected the proximal and distal fragments. Preliminary evaluation by the surgeon (Professor Milgrom) of the modeling, validation, visualization, and preoperative planning indicates satisfactory results and ease of use.

To validate the fluoroscopic image-processing modules, we conducted a series of experiments with two Phillips BV 25 C-arm units with 9-inch field of view (Phillips, The Netherlands). The images were transferred from the fluoroscope's video output port to the computer using an external frame

Table 1. Dewarp Map Results Showing Distance Variation of 348 Pairs of Furthest Center Points for Different C-Arm Pitch and Yaw Orientations

Pose Angle	Mean	SD	Min	Max
(0, −10)	0.381	0.201	0	0.890
(0, 10)	0.415	0.205	0	0.937
(0, −15)	0.390	0.203	0	0.991
(0, 15)	0.313	0.193	0	0.838
(10, 15)	0.489	0.211	0	0.946
(10, −15)	0.344	0.201	0	0.913
(−10, 15)	0.301	0.193	0	0.870
(0, 90)	1.931	0.541	0	2.917
(80, 0)	2.708	0.861	0	4.219
(0, 180)	2.550	0.703	0	3.717

All distance measurements are in millimeters relative to the pose angle yaw = 0°; pitch = 0°.

grabber (Grabit; AIMS) with a resolution of 720 × 560 and pixel size of 0.44 mm. At the Precision Mechanics Laboratory, the Hebrew University of Jerusalem, we built a custom dewarping grid and calibration object which is fitted via existing screw holes to the image intensifier plate. The designs are inexpensive, simple to manufacture, and lightweight, to minimize additional C-arm deflection.

The dewarping grid is a 7-mm-thick coated aluminum alloy plate with 405 4-mm-diameter holes uniformly distributed at 10-mm intervals machined to 0.02-mm precision. It is simpler and cheaper to make than the commonly used steel balls mounted on a radiolucent plate, and yields similar results. The calibration object (Fig. 10) is a hollow Delrin™ three-step cylinder with 18 5-mm-diameter steel balls in three parallel planes angularly distributed to avoid overlap in the image. An additional ball in the top circular face marks the center of the object. A rectangular bar, affixed to the bottom of the cylinder, has holes that allow mounting the object directly on the image intensifier plate. The balls are mounted at heights of 20, 100, and 180 mm from the cylinder base, forming circles of 130, 115, and 90 mm diameter, respectively. The object weighs 1.5 kg.

To determine the intrinsic accuracy and repeatability error of the system, we acquired five series of images of the dewarping grid at a fixed C-arm orientation and exposure. We observed small relative rigid motion between shots introduced by the frame grabber. We correct for this motion in all our images by shifting the image pixels so that the center of the fluoroscope's circular field of view is always in the same position. This image shift correction is necessary so that it is not wrongly interpreted as a physical displacement; a perfectly static bone will appear to have moved owing to the shift. Once this shift was corrected, we measured the distances between matching hole centers in pairs of images. For 1389 measurements, mean error = 0.038 mm, with standard deviation (σ) = 0.032 mm, minimum = 0.001 mm, and maximum = 0.227 mm. Since the error is almost an order of magnitude smaller than other errors, we conclude that there is no need to take several exposures and average between them, as in Schreiner et al.[33]

To quantify how sensitive the dewarp map is to changes in C-arm orientations, and thus determine how many predetermined orientations must be captured, we computed distortion maps at different orientations. Table 1 summarizes the results. We observe a significant point center shift of up to 4 mm between extreme C-arm orientations, and of almost 1 mm for orientations 15° apart. To determine the accuracy of the dewarp map function on new images, we acquired an image of the grid attached to the image intensifier cover at a fixed C-arm orientation and computed the dewarp map. Then we detached the grid, placed it at an arbitrary angle on the cover, acquired a new image, and corrected it with the dewarp map (Fig. 9). We located the image hole centers in the new dewarped image with the hole segmentation routine and computed a worst-case error bound by taking the relative distances between pairs of points that were furthest apart. For 30 measurements, the mean error was 0.104 mm, with σ = 0.060 mm, minimum = 0.007 mm, and maximum = 0.198 mm. Previous studies report similar residual errors after correction.[2,29]

Table 2. Calibration Parameter Nominal Values and Sensitivity to C-Arm Orientation

Parameter	Mean	SD	Min	Max
T_x (mm)	0	0.882	−1.300	1.185
T_y (mm)	0	0.251	−0.317	0.339
R_x (deg)	0	0.342	−0.393	0.348
R_y (deg)	0	0.145	−0.233	0.169
R_z (deg)	0	0.213	−0.407	0.170
T_z (mm)	915.756	15.129	891.825	929.508
f	48.598	0.772	47.433	49.402
C_x	257.544	0.182	257.289	257.760
C_y	203.815	0.085	203.699	203.960
κ	0.00013	0.00001	0.00012	0.00015
s	1.00032	1.00283	1.00165	0.0009

The extrinsic parameters T and R are with respect to a coordinate frame on the center of the image intensifier. The absolute values of the first five parameters are unimportant; only their relative variation matters.

To determine the calibration parameter variation for the different C-arm orientations, we conducted measurements for six extreme orientations. Table 2 summarizes the results. Note that the variation in T_z, which measures the distance between the camera pinhole and the image plane, was significant and confirmed the deflection of the C arm.[16] The small radial distortion and scaling deviations showed that the dewarping procedure was very accurate. To quantitatively validate the accuracy of the calibration, we imaged the calibration object and computed the calibration parameters. We then constructed the projection matrix and used it to compute the geometric coordinates of the ball centers. For each ball, we computed the distance between the geometric and the image coordinate centers. The mean distance error for 78 measurements was 0.201 mm with $\sigma = 0.089$ mm, minimum = 0.033 mm, and maximum = 0.449 mm.

We conducted a preliminary evaluation of the contour extraction algorithm on three sets of fluoroscopic images taken from actual surgeries. The global and local gradient image threshold percentiles (lower = 60%; upper = 94.7%; lower = 60 %; upper = 99%), window size (13×13 pixels^2), and number of neighbors ($n = 4$) were kept constant for all images in a session.

Figure 11 shows typical results. Note that there were very few outliers, which could be removed with a simple model-based scheme or by combining segmentation and registration, as in Hamadeh et al.[14]

DISCUSSION

Current fluoroscopy-based orthopedic procedures have the disadvantage of cumulative radiation exposure to the surgeon and impose a mental burden on the surgeon, who has to correlate the fluoroscopic images to coordinate his visual and mechanical reference frames when performing surgical gestures. This lack of registration of sensory information leads to positioning errors and complications in a non-negligible number of cases, and contributes to a long learning curve in acquiring skills.

Our goal in developing the FRACAS system was to overcome these limitations by providing a system that replaces fluoroscopic images with a virtual reality display of 3D bone models created from preoperative CT and tracked intraoperatively in real time. Fluoroscopic images are used to register the bone models to the intraoperative situation and to verify that the registration is maintained. We have satisfactorily tested the modeling, preoperative planning, and visualization modules on six clinical cases. For fluoroscopic image processing, our experiments suggest that, after dewarping and calibration, submillimetric spatial positioning accuracy possibly better than 0.5 mm is achievable with standard equipment. Preliminary contour segmentation results show good contour tracing with very few outliers. These can be removed with a simple model-based scheme or by combining segmentation and registration.[14]

The key advantages of FRACAS are that it provides an integrated solution to intramedullary nailing and it uses fluoroscopic images to perform anatomy-based registration without requiring direct contact between the tracker tools and the patient's anatomy. However, it requires a preoperative CT study, additional equipment, and a separate procedure for C-arm calibration. We believe that these disadvantages will be outweighed by the benefits in reduced radiation, reduced complications, and improved accuracy.

Our current work focuses on completing the registration module and integrating the system modules to obtain a working prototype of the whole system. We are also developing a hardware simulator to carry out *in vitro* accuracy and ergonomy experiments. We are also considering closely related clinical applications including intramedullary nailing of the tibia and humerus.

ACKNOWLEDGMENTS

Leo Joskowicz was supported by a Guastalla Faculty Fellowship and a grant from the Israel Ministry of Industry and Trade–IZMEL Consortium on Image-Guided Therapy, and, together with Charles Milgrom, by Equipment Grant 9061/98 from the Israel Academy of Sciences and Humanities. Lana Tockus was supported by a Silicon Graphics Biomedical (now Biomedicom) grant. The authors also acknowledge the contribution of students Ofri Sadowski and Guy Leshem, who recently joined the project.

REFERENCES

1. Besl PJ, McKay ND. A method for registration of 3D shapes. IEEE Trans Pattern Anal Machine Intell 1992; 14:239–256.
2. Brack C, Burghart R, Czpof A, et al. Accurate X-ray navigation in computer-assisted surgery. In: Lemke H et al., editor. Proceedings of the 12th International Symposium on Computer Assisted Radiology and Surgery (CAR '98). New York: Elsevier; 1998. p 716–722.
3. Brumback RJ. Regular and special features—the ra-

tionales of interlocking nailing of the femur, tibia, and humerus. Clin Orthop Rel Res 324:292–320.
4. Carrat L, Tonetti J, Lavallée S, Merloz P, Pittet L, Chirossel JP. Treatment of pelvic ring fractures: Percutaneous computer-assisted illiosacral screwing. In: Wells S et al., editors. Proceedings of the 1st International Conference on Medical Computing and Computer-Assisted Intervention. Lecture Notes in Com puter Science Vol. 1496. New York: Elsevier; 1998. p 84–91.
5. Davies B, Harris SJ, Lin WJ, Hibberd RD, Middleton R, Cobb JC. Active compliance in robotic surgery—the use of force as a dynamic constraint. Proc Inst Mech Eng 1997;211:285–292.
6. Ellis RE, Fleet DJ, Bryant JT, Rudan J, Fenton P. A method for evaluating CT-based surgical registration. In: Troccaz J et al., editors. CVRMed-MRCAS '97. Lecture Notes in Computer Science Vol. 1205. New York: Springer; 1997. p 141–150.
7. Fadda M, Bertelli D, Martelli S, Marcacci M., Dario P, Carmella D, Trippi D. Computer assisted planning for total knee arthroplasty. In: Troccaz J et al., editors. CVRMed-MRCAS '97. Lecture Notes in Computer Science Vol. 1205. New York: Springer, 1997. p 619–628.
8. Fahrig R, Moreau M, Holdsworth DW. Three-dimensonal computed tomographic reconstruction using a C-arm mounted XRII: Correction of image intensifier distortion. Med Phys 1997;24:1097–1106.
9. Garza-Jinich M, Meer P, Medina V. Robust retrieval of 3D structures from magnetic resonance images. In: Proceedings of the Conference on Pattern Recognition. Piscataway, NJ: IEEE Press, p 1–21.
10. Glossop N, Hu R. Distal hole targeting in intramedullary nails. In: Third Annual Symposium on Computer Assisted Orthopaedic Surgery, Bern, Switzerland, 1997. p 32–39.
11. Glossop N, Hu R. Clinical use accuracy in image guided surgery. In: Proceedings of the 11th International Symposium on Computer Assisted Radiology and Surgery (CAR '97), Berlin. New York: Elsevier; 1997. p 889–893.
12. Glossop N, Hu R. Effect of registration method on clinical accuracy of image guided pedicle screw surgery. In: Proceedings of the 11th International Symposium on Computer Assisted Radiology and Surgery (CAR '97), Berlin. New York: Elsevier; 1997. p 884–888.
13. Guéziec A, Kazanzides P, Williamson B, Taylor RH, Lord D. Anatomy based registration of CT-scan and X-ray fluoroscopy data for intra-operative guidance of a surgical robot. IEEE Trans Med Imaging 1998;17: 410–419.
14. Hamadeh A, Sautot P, Lavallée S, Cinquin P. Towards automatic registration between CT and X-ray images: Cooperation between 3D/2D registration and 2D edge detection. In Proceedings of the Second International Symposium on Medical Robotics and Computer Assisted Surgery, 1995. p 39–46.
15. Hamadeh A, Lavallée S, Cinquin P. Automated 3-dimensional computer tomographic and fluoroscopic image registration. Comput Aided Surg 1998;3:11–19.
16. Hofstetter R, Slomczykowski M, Bourquin I, Nolte LP. Fluoroscopy based surgical navigation—concept and clinical applications. In: Lemke HU et al., editors. Proceedings of the 11th International Symposium on Computer Assisted Radiology and Surgery (CAR '97). New York: Elsevier; 1997. p 956–960.
17. Hu R, Glossop N, Steven D, Randle J. Accuracy of image guided placement of iliosacral lag screws. In: Troccaz J et al., editors. Proceedings of CVRMed-MRCAS '97. Lecture Notes in Computer Science Vol. 1205. New York: Springer; 1997. p 593–596.
18. Joskowicz L, Taylor RH, Williamson B, Kane R, Kalvin A, Guéziec A, Taubin G, Funda J, Gomory S, Brown L, McCarthy J, Turner R. Computer-integrated revision total hip replacement surgery: Preliminary report. In: Second International Symposium on Medical Robotics and Computer Assisted Surgery. Baltimore: Wiley; 1995. p 193–202.
19. Joskowicz L, Tockus L, Yaniv Z, Simkin A, Milgrom C. Computer-aided image-guided bone fracture surgery—concept and implementation. In: Lemke HU et al., editors. Proceedings of the 12th International Symposium on Computer Assisted Radiology and Surgery (CAR '98). New York: Elsevier; 1998. p 710–715.
20. Koppe R, Klotz E, Op de Beek J, Aerts H. 3D vessel reconstruction based on rotational angiography. In: Proceedings of the 9th International Symposium on Computer Assisted Radiology (CAR '95). New York: Springer; 1995. p 101–107.
21. Langlotz F, Bächer R, Sati M, Berlemann U, et al. Computer assistance for pelvic osteotomies. Clin Orthop (in press).
22. Lavallée S, Sautot P, Troccaz J, Cinquin P, Merloz P. Computer assisted spine surgery: A technique for accurate transpedicular screw fixation using CT data and a 3D optical localizer. J Image Guided Surg 1995;1: 65–73.
23. Lavallée S, Szeliski R, Brunie L. Anatomy-based registration of three-dimensional medical images, range images, X-ray projections, and three-dimensional models using octree-splines. In: Taylor RH, Lavallée S, Burdea G, Mösges R, editors. Computer Integrated Surgery: Technology and Clinical Applications. Boston: MIT Press; 1995. p 115–143.
24. Lavallée S, Troccaz J, Sautot P, Mazier B, Cinquin P, Merloz P, Chirossel JP. Computer-assisted spinal surgery using anatomy-based registration. In: Taylor RH, Lavallée S, Burdea G, Mösges R, editors. Computer Integrated Surgery: Technology and Clinical Applications. Boston: MIT Press;1995. p 425–449.
25. Leitner F, Picard F, Minfelde R, Schultz HJ, Cinquin P, Saragaglia D. Computer-assisted knee surgical total replacement. In: Troccaz J et al., editors. Proceedings

of CVRMed-MRCAS '97. Lecture Notes in Computer Science, Vol. 1205. New York: Springer; 1997. p 629–637.
26. Lorensen WE, Cline HE. Marching cubes: A high resolution 3D surface construction algorithm. SIGGRAPH '87 1987;21:163–169.
27. Li QH, Holdener HJ, Zamorano L, Nolte LP, Visarius H, Diaz F. Computer-assisted transpedicular screw insertion. In: Lecture Notes in Computer Science. New York: Springer; 1996. p 328–335.
28. Nolte LP, Visarius H, Arm E, Langlotz F, Schwarzenbach O, Zamorano L. Computer-aided fixation of spinal implants. J Image Guided Surg 1995;1:88–93.
29. Ozanian T, Phillips R, Viant W, Moshen A, Sherman K, Cain T. Automatic feature detection in X-ray images for planning a drilling trajectory in orthopaedic surgery. In: Proceedings of the Medical Image Understanding and Analysis Conference (MIAU '97), 1997. p 113–116.
30. Phillips R, Viant WJ, Moshen AMMA, Griffiths JG, Bell MA, Cain TJ, Sherman KP, Karpinski MRK. Image guided orthopaedic surgery: Design and analysis. Trans Inst Measure Control 1995;17:251–265.
31. Russel TA. Fractures of lower extremity. In: Campbell's orthopaedic encyclopedia; 1995. p 785–885.
32. Sanders R. Exposure of the orthopaedic surgeon to radiation. J Bone Joint Surg 1993;75A:326–330.
33. Schreiner S, Funda J, Barnes AC, Anderson JH. Accuracy assessment of a clinical biplane fluoroscope for three-dimensional measurements and targeting. Proc SPIE Med Imaging, 1995. p 321–328.
34. Simon DA. Techniques for fast and accurate intra-surgical registration. J Image Guided Surg 1995;1:17–29.
35. Simon DA, Jaramaz B, Blackwell M, Morgan F, DiGioia AM, Kischell E, Colgan B, Kanade T. Development and validation of a navigational guidance system for acetabular implant placement. In: Proceedings of CVRMed-MRCAS '97. Lecture Notes in Computer Science, Vol. 1205. New York: Springer, 1995. p 583–592.
36. Taylor RH, Mittelstadt BD, Paul HA, Hanson W, Kazanzides P, Zuhars JF, Williamson B, Musits BL, Glassman E, Bargar WL. An image-directed robotic system for precise orthopaedic surgery. IEEE Trans Robotics Automation 1994;10:261–275.
37. Taylor RH, Joskowicz L, Williamson B, et al. Computer integrated revision total hip replacement surgery. Med Image Anal (in press).
38. Tockus L. A system for computer-aided image-guided bone fracture surgery: modeling, visualization, and preoperative planning. MSc thesis, Hebrew University, Jerusalem; 1997.
39. Tockus L, Joskowicz L, Simkin A, Milgrom C. Computer-aided image-guided bone fracture surgery: Modeling, visualization, and preoperative planning. In: Wells S et al., editors. First International Conference on Medical Computing and Computer-Assisted Intervention. Lecture Notes in Computer Science, Vol. 1496. New York: Elsevier; 1998. p 29–38.
40. Tsai R. A versatile camera calibration technique for high-accuracy 3D machine vision metrology using off-the-shelf TV cameras and lenses. IEEE J Robotics Automation 1998;RA-3:323–344.
41. Viant WJ, Phillips R, Griffiths JG, et al. A computer assisted orthopaedic system for distal locking of intramedullary nails. Proc Inst Mech Eng 1997;211(H): 1–8.
42. Woods RE, Gonzalez RC. Digital Image Processing. New York: Addison-Wesley; 1992.
43. Yaniv Z, Joskowicz L, Simin A, Garza-Jinich M, Milgrom. Fluoroscopic image processing for computer-aided orthopaedic surgery. In: Wells S et al., editors. First International Conference on Medical Computing and Computer-Assisted Intervention. Lecture Notes in Computer Science, Vol. 1496. New York: Elsevier; 1998. p 325–334
44. Yaniv Z. Fluoroscopic image processing and registration for computer-aided orthopaedic surgery. MSc thesis, Hebrew University, Jerusalem; 1998.